Research Article | Vol. 9, No. 2 | 1 Feb 2018 | BIOMEDICAL OPTICS EXPRESS 387
Biomedical Optics EXPRESS

Coherent anti-Stokes Raman scattering rigid endoscope toward robot-assisted surgery

K. Hirose,[1] T. Aoki,[1] T. Furukawa,[2] S. Fukushima,[1] H. Niioka,[1] S. Deguchi,[1] and M. Hashimoto[3,*]

[1]Graduate School of Engineering Science, Osaka University, Osaka, Japan
[2]Faculty of Engineering, Yokohama National University, Yokohama, Japan
[3]Graduate School of Information Science and Technology, Hokkaido University, Hokkaido, Japan
[*]hashimoto@ist.hokudai.ac.jp

Abstract: Label-free visualization of nerves and nervous plexuses will improve the preservation of neurological functions in nerve-sparing robot-assisted surgery. We have developed a coherent anti-Stokes Raman scattering (CARS) rigid endoscope to distinguish nerves from other tissues during surgery. The developed endoscope, which has a tube with a diameter of 12 mm and a length of 270 mm, achieved 0.91% image distortion and 8.6% non-uniformity of CARS intensity in the whole field of view (650 μm diameter). We demonstrated CARS imaging of a rat sciatic nerve and visualization of the fine structure of nerve fibers.

OCIS codes: (170.2150) Endoscopic imaging; (170.5660) Raman spectroscopy; (170.3890) Medical optics instrumentation.(170.0110) Imaging systems.

References and links

1. A. Tewari, A. Srivastava, and M. Menon, "A prospective comparison of radical retropubic and robot-assisted prostatectomy: experience in one institution," BJU International **92**(3), 205–210 (2003).
2. Q. D. Trinh, J. Sammon, M. Sun, P. Ravi, K. R. Ghani, M. Bianchi, W. Jeong, S. F. Shariat, J. Hansen, J. Schmitges, C. Jeldres, C. G. Rogers, J. O. Peabody, F. Montorsi, M. Menon, and P. I. Karakieeq.wicz,"Perioperative Outcomes of Robot-Assisted Radical Prostatectomy Compared With Open Radical Prostatectomy: Results From the Nationwide Inpatient Sample," European Urology **61**(4), 679–685 (2012).
3. B. H. Bochner, G. Dalbagni, D. D. Sjoberg, J. Silberstein, Gal E. Keren Paz, S. M. Donat, J. A. Coleman, S. Mathew, A. Vickers, G. C. Schnorr, M. A. Feuerstein, B. Rapkin, R. O. Parra, H. W. Herr, and V. P. Laudone, "Comparing Open Radical Cystectomy and Robot-assisted Laparoscopic Radical Cystectomy: A Randomized Clinical Trial.," European Urology **67**(6), 1042–1050 (2015).
4. H. Becker, A. Melzer, M. Oliver Schurr, and G. Buess, "3-D video techniques in endoscopic surgery," Endoscopic surgery and allied technologies **1**(1), 40–46 (1993).
5. M. Menon, S. Kaul, A. Bhandari, A. Shrivastava, A. Tewari, and A. Hemal, "Potency Following Robotic Radical Prostatectomy: A questionnaire Based Analysis of Outcomes After Conventional Nerve Sparing and Prostatic Fascia Sparing Techniques," The Journal of Urology **174**(6), 2291–2296 (2005).
6. U. Michl, P. Tennstedt, L. Feldmeier, P. Mandel, S. J. Oh, S. Ahyai, L. Budäus, F. K.H. Chun, A. Haese, H. Heinzer, G. Salomon, T. Schlomm, T. Steuber, H. Huland, M. Graefen, and D. Tilki, "Nerve-sparing Surgery Technique, Not the Preservation of the Neurovascular Bundles, Leads to Improved Long-term Continence Rates After Radical Prostatectomy," European Urology **69**(4), 584–589 (2016).
7. K. D. Sievert, J. Hennenlotter, I. A. Laible, B. Amend, U. Nagele, and A. Stenzl, "The Commonly Performed Nerve Sparing Total Prostatectomy Does Not Acknowledge the Actual Nerve Courses," The Journal of Urology **181**(3), 1076–1081 (2009).
8. A. Takenaka, A. Tewari, R. Hara, R.A. Leung, K. Kurokawa, G. Murakami, and M. Fujisawa, "Pelvic autonomic nerve mapping around the prostate by intraoperative electrical stimulation with simultaneous measurement of intracavernous and intraurethral pressure," Journal of Urology **177**(1), 225–229 (2007).
9. M. A. Whitney, J. L. Crisp, L. T. Nguyen, B. Friedman, L. A. Gross, P. Steinbach, R. Y. Tsien, and Q. T. Nguyen, "Fluorescent peptides highlight peripheral nerves during surgery in mice," Nature Biotechnology **29**(4), 352–356 (2011).
10. T. Minamikawa, Y. Harada, N. Koizumi, K. Okihara, K. Kamoi, A. Yanagisawa, and T. Takamatsu, "Label-free detection of peripheral nerve tissues against adjacent tissues by spontaneous Raman microspectroscopy," Histochemistry and Cell Biology **139**(1), 181–193 (2013).
11. T. Minamikawa, Y. Harada, and T. Takamatsu, "Ex vivo peripheral nerve detection of rats by spontaneous Raman spectroscopy," Scientific Reports **5**, 17165 (2015).

#312954 https://doi.org/10.1364/BOE.9.000387
Journal © 2018 Received 10 Nov 2017; revised 16 Dec 2017; accepted 18 Dec 2017; published 2 Jan 2018

Biomedical Optics EXPRESS

12. Y. Kumamoto, Y. Harada, H. Tanaka, and T. Takamatsu, "Rapid and accurate peripheral nerve imaging by multipoint Raman spectroscopy," Scientific Reports **7**, 845 (2017).
13. S. Kaminaka, T. Ito, H. Yamazaki, E. Kohda, and H. Hamaguchi, "Near-infrared multichannel Raman spectroscopy toward real-time in vivo cancer diagnosis," Journal of Raman Spectroscopy **33**(7), 498–502 (2002).
14. M. S. Bergholt, W. Zheng, K. Lin, K. Y. Ho, M. Teh, K. G. Yeoh, J. B. Y. So, and Z. Huang, "In Vivo Diagnosis of Esophageal Cancer Using Image-Guided Raman Endoscopy and Biomolecular Modeling," Technology in Cancer Research & Treatment **10**(2), 103–112 (2011).
15. T. B. Huff and J. X. Cheng "In vivo coherent anti-Stokes Raman scattering imaging of sciatic nerve tissue," Journal of Microscopy **225**(2), 175–182 (2007).
16. L. Gao, H. Zhou, M. J. Thrall, F. Li, Y. Yang, Z. Wang, P. Luo, K. K. Wong, G. S. Palapattu, and S. T. C. Wong, "Label-free high-resolution imaging of prostate glands and cavernous nerves using coherent anti-Stokes Raman scattering microscopy," Biomed. Opt. Express **2**(4), 915–926 (2011).
17. F. Tian, W. Yang, D. A. Mordes, J. Y. Wang, J. S. Salameh, J. Mok, J. Chew, A. Sharma, E. Leno-Duran, S. S. Uematsu, N. Suzuki, S. S. Han, F. K. Lu, M. Ji, R. Zhang, Y. Liu, J. Strominger, N. A. Shneider, L. Petrucelli, X. S. Xie, and K. Eggan, "Monitoring peripheral nerve degeneration in ALS by label-free stimulated Raman scattering imaging," Nature Communications **7**, 13283 (2016).
18. C. L. Evans, E. O. Potma, M. Puoris'haag, D. Côté, C. P. Lin, and X. S. Xie, "Chemical imaging of tissue in vivo with video-rate coherent anti-Stokes Raman scattering microscopy," Proc. Nat. Acad. Sci. USA **102**(46), 16807–16812 (2005).
19. T. Minamikawa, M. Hashimoto, K. Fujita, S. Kawata, and T. Araki, "Multi-focus excitation coherent anti-Stokes Raman scattering (CARS) microscopy and its applications for real-time imaging," Optics Express **17**(12), 9526–9536 (2009).
20. B. G. Saar, C. W. Freudiger, J. Reichman, C. M. Stanley, G. R. Holtom, and X. S. Xie, "Video-Rate Molecular Imaging in Vivo with Stimulated Raman Scattering," Science **330**(6009), 1368–1370 (2010).
21. Y. Ozeki, W. Umemura, Y. Otsuka, S. Satoh, H. Hashimoto, K. Sumimura, N. Nishizawa, K. Fukui, and K. Itoh, "High-speed molecular spectral imaging of tissue with stimulated Raman scattering," Nature Photonics **6**, 845–851 (2012).
22. F. Légaré, C. L. Evans, F. Ganikhanov, and X. S. Xie, "Toward CARS Endoscopy," Opt. Express **14**(10), 4427–4432 (2006).
23. M. Balu, G. Liu, Z. Chen, B. J. Tromberg, and E. O. Potma, "Fiber delivered probe for efficient CARS imaging of tissues," Opt. Express **18**(3), 2380–2388 (2010).
24. B. G. Saar, R. S. Johnston, C. W. Freudiger, X. S. Xie, and E. J. Seibel, "Coherent Raman scanning fiber endoscopy," Optics Letters **36**(13), 2396–2398 (2011).
25. B. Smith, M. Naji, S. Murugkar, E. Alarcon, C. Brideau, P. Stys, and H. Anis, "Portable, miniaturized, fibre delivered, multimodal CARS exoscope," Opt. Express **21**(14), 17161–17175 (2013).
26. X. Cheng, X. Xu, D. T. McCormick, K. Wong, and S. T.C. Wong, "Multimodal nonlinear endo-microscopy probe design for high resolution, label-free intraoperative imaging," Biomed. Opt. Express **6**(7), 2283–2293 (2015).
27. A. Lukic, S. Dochow, H. Bae, G. Matz, I. Latka, B. Messerschmidt, M. Schmitt, and J. Popp, "Endoscopic fiber probe for nonlinear spectroscopic imaging," Optica **4**(5), 496–501 (2017).
28. A. Lombardini, V. Mytskaniuk, S. Sivankutty, E. R. Andresen, X. Chen, J. Wenger, M. Fabert, N. Joly, F. Louradour, A. Kudlinski, and H. Rigneault, "High-resolution multimodal flexible coherent Raman endoscope," https://arxiv.org/abs/1708.04149.
29. G. T. Sung and I. S. Gill, "Robotic laparoscopic surgery: a comparison of the da Vinci and Zeus systems," Urology **58**(6), 893–898 (2001).
30. T. Minamikawa, N. Tanimoto, M. Hashimoto, and T. Araki, "Jitter reduction of two synchronized picosecond mode-locked lasers using balanced cross-correlator with two-photon detectors ," Applied Physics Letters **89**(19), 191101 (2006).
31. H. Cahyadi, J. Iwatsuka, T. Minamikawa, H. Niioka, T. Araki, and M. Hashimoto, "Fast spectral coherent anti-Stokes Raman scattering microscopy with high-speed tunable picosecond laser," J. Biomed. Opt. **18**(9), 096009 (2013).
32. Y. Takagi, T. Kobayashi, K. Yoshihara, and S. Imamura, "Multiple- and single-shot autocorrelator based on two-photon conductivity in semiconductors," Opt. Lett. **17**(9), 658–660 (1992).
33. J. K. Ranka, and A. L. Gaeta, "Autocorrelation measurement of 6-fs pulses based on the two-photon-induced photocurrent in a GaAsP photodiode," Opt. Lett. **22**(17), 1344–1346 (1997).
34. E. Bélanger, S. Bégin, S. Laffray, Y. D. Koninck, R. Vallée, and D. C. Côté, "Quantitative myelin imaging with coherent anti-Stokes Raman scattering microscopy: alleviating the excitation polarization dependence with circularly polarized laser beams," Opt. Express **17**(21), 18419–18432 (2009).
35. M. Born, and E. Wolf, *Principles of Optics,* 6th ed. (Cambridge university press, 1980), Chap. 8.

1. Introduction

Robot-assisted surgery has become a standard method for the treatment of cancer. Advantages of robot-assisted surgery include less burden on the patient and less bleeding as compared to

Biomedical Optics EXPRESS

traditional open surgery, resulting in improved quality of life (QoL) [1–3]. Under robot-assisted surgery, surgeons observe high-resolution, high-magnification, depth perception images provided by a video camera in a rigid endoscope [4]. However, surgeons must determine the extent of resection by recognizing subtle absorption differences of visible light and utilizing anatomical knowledge. For instance, surgeons performing robot-assisted laparoscopic prostatectomy are expected to excise the prostate gland without injuring the surrounding nervous plexus because preservation of neurological function is required for avoiding erectile dysfunction and achieving early recovery of urinary function [5, 6]. Although relatively thick, visible nerves, such as neurovascular bundles, have been targeted and preserved, invisible nerves that also play an important role for urinary function are often overlooked and removed with the prostate gland [7]. Therefore, intraoperative nerve visualization for use with endoscopic robots will undoubtedly improve the QoL of patients.

Several methods have been proposed and demonstrated for visualizing and/or identifying nerves. Electrical stimulation is used for the identification of motor nerves [8]. However, this method cannot be applied to the identification of sensory and autonomic nerves. Although dye-based techniques are useful for the visualization of nerves [9], toxicity and specificity are often serious issues for medical applications. To overcome these issues, recently, label-free nerve identification using spontaneous Raman scattering spectroscopy and imaging has been investigated [10].

Raman scattering provides information about molecular vibrations and is highly sensitive to the biological molecular species. Label-free identification and mapping of myelinated nerves, unmyelinated nerves, adipose tissue, and fibrous connective tissue of peri-prostatic tissue by the analysis of Raman spectra has been demonstrated [10, 11]. Moreover, to achieve rapid, accurate detection of peripheral nerves, 32-point Raman scattering spectroscopy by using a microlens array has been proposed, and high specificity and accuracy for nerve detection has been shown [12]. Flexible Raman endoscopes have also been developed and applied to cancer detection [13, 14]. Although spontaneous Raman endoscopy has been shown to be useful for intraoperative measurements, the low intensity of spontaneous Raman scattering limits this technique to single-point detection.

Coherent Raman scattering (CRS) imaging techniques have attracted much interest for high-speed imaging of biological tissues. Imaging techniques based on CRS, such as coherent anti-Stokes Raman scattering (CARS) and stimulated Raman scattering (SRS), have been proposed for visualizing nerves without staining [15–17]. CRS employs two-color pulsed lasers: a pump beam (ω_p) and a Stokes beam (ω_s). When the frequency difference between the pump and Stokes beams coincides with a molecular vibration ($\Omega = \omega_p - \omega_s$), non-linear Raman effects of CARS and SRS are induced. Since the CARS and SRS signals are much larger than that of spontaneous Raman scattering, video-rate imaging of biological tissue has been reported [18–21]. Using CRS microscopy, myelinated nerves were visualized by exciting CH_2 bonds derived from lipids within myelin sheaths [15–17]. CRS microscopy is a powerful method for label-free nerve imaging. Recently, several groups have investigated miniature and/or flexible fiber CRS imaging systems for clinical use [22–28]. On the other hand, for robot-assisted surgery, inserted part into the human body should be small diameter (typically smaller than 12 mm diameter) [29], but flexibility of the inserted part is not required. In this paper, we describe the development of a CARS rigid endoscope as a new portable label-free nerve imaging tool toward robot-assisted surgery.

2. Development of CARS rigid endoscope system

A CARS rigid endoscope must have the following four features: two synchronized ultrafast pulsed lasers with different colors, an optical fiber connecting the lasers and the endoscope for achieving portability, a small-diameter endoscope tube to easily access the surgical region, and an imaging

Biomedical Optics EXPRESS

system for visualization.

Two ultrafast pulsed lasers are required to generate a CARS signal and are spatially and temporally overlapped with high accuracy. Since the excitation laser sources are highly sensitive to atmospheric fluctuations or vibrations, they must be separated from the endoscope head. The endoscope head must also be portable. We use an optical fiber to deliver the two laser beams to the head. In the rigid endoscope, a lens tube with small diameter is used to decrease the physical burden on the patient. Finally, a beam scanning and epi-detection system are required for CARS endoscopy. Since CARS is a non-linear optical process, the laser beams must be focused at the same point and two-dimensionally scanned to obtain an image.

The schematic optical design of the developed CARS rigid endoscope system is shown in Fig. 1(a). The system consists of synchronized pulsed lasers with different wavelengths (ω_p, ω_s), a single-mode fiber (SMF), a reflective fiber collimator, and a rigid endoscope head. A picosecond mode-locked Ti:sapphire laser (repetition rate = 80 MHz, Tsunami, Spectra-Physics) and a picosecond acoustic-tunable optic-filter (AOTF) mode-locked Ti:sapphire laser (repetition rate = 80 MHz, Megaopt) operated at different wavelengths are used as light sources. The wavelengths of the two pulses are set to 709 nm and 888 nm to visualize lipids of nerves within myelin sheaths using CH_2 symmetric stretching at a Raman shift of 2845 cm^{-1}. The two pulses are temporally synchronized with a synchronization system described previously [19, 30, 31], and the temporal time difference is adjusted with an optical delay (Mark-202, Sigmakoki). The two pulses are coupled into a single-mode fiber (SMF; P1-630A-FC-2, Thorlabs) using a reflective fiber collimator (FC1; RC04FC-P01, Thorlabs), and the delivered pulses are coupled out and collimated with a reflective fiber collimator (FC2; exit beam radius = 1 mm, RC02FC-P01, Thorlabs). In the rigid endoscope head, the two pulses travel to the sample plane through a beam splitter (BS), a scanning system implemented by galvanometer mirrors (GVS002, Thorlabs) for XY scanning, and a rigid endoscope tube. Backscattered CARS is detected with a photomultiplier tube (PMT; C9110, Hamamatsu). Reflection light and transmission lights are also detected with silicon photodiodes (PD2, PD3).

As shown in Fig. 1(c) and (d), the tube of the CARS rigid endoscope (diameter = 12 mm, length = 270 mm) consists of cylinders, a pair of relay lenses (RL; f = 75 mm, TS achromatic lens 9×75 VIS-NIR INK, Edmund), and an achromatic objective lens (OB; f = 7.5 mm, AC050-008-B-ML, Thorlabs). As shown in Fig. 1(d), three types of cylinders, namely, outer cylinders (outer diameter = 12 mm, inner diameter = 9 mm), inner cylinders (outer diameter = 9 mm, inner diameter = 7 mm), and a cap cylinder (outer diameter = 12 mm, inner diameter = 7mm), are used to fix the positions of the relay lenses. As shown in Fig. 1(e), in the current setup (beam radius = 1.0 mm), the numerical aperture is 0.13.

3. Evaluation of developed system

3.1. Group delay difference between two laser pulses in optical fiber

In order to obtain the CARS signal, the two color laser pulses must be temporally and spatially overlapped on the sample. Since the two laser beams are combined and then delivered using a single-mode fiber, spatial overlapping is guaranteed at least on the output end face of the fiber. To confirm temporal overlapping on the sample, the cross-correlation of the two pulses was observed. Figure 2 shows cross-correlation signals of the two laser pulses observed before introducing the single-mode fiber (PD1 in Fig. 1(a)) and at the sample (PD3) position by scanning the optical delay. The wavelengths of the pump and Stokes beams were set to 709 and 888 nm, respectively. Cross-correlation signals were observed with two-photon detectors (TPDs). Since the TPDs were photodiodes made of a wide band gap semiconductor (GaAsP: G1115, Hamamatsu), they were insensitive to single-photon absorption of the Ti:sapphire laser light but were sensitive to two-photon absorption [32, 33]. As a result of two-photon absorption, the current from the photodiodes was proportional to the square of the laser power, and the intensity

Biomedical Optics EXPRESS

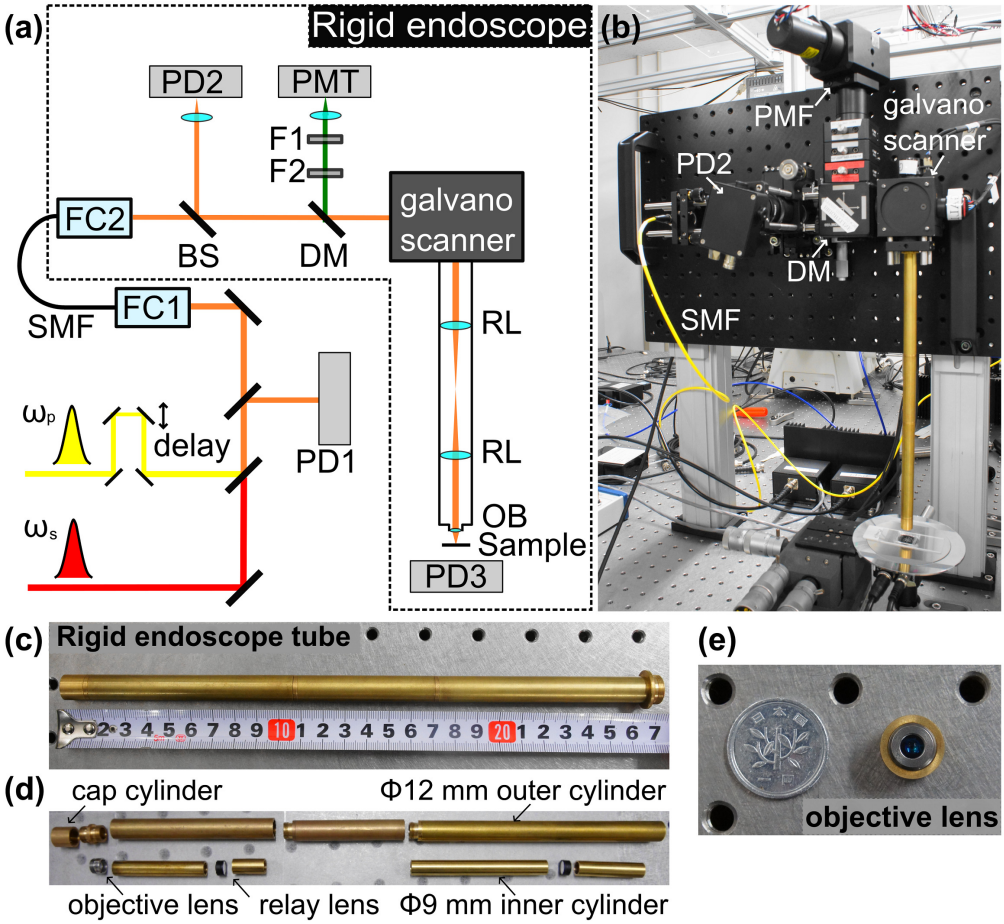

Fig. 1. The CARS rigid endoscope system. (a) Schematic optical design of the CARS rigid endoscope system. Two synchronized picosecond mode-locked Ti:sapphire laser pulses are delivered by a single-mode fiber (SMF) and collimated by a reflective fiber collimator 2 (FC2). The two pulses are focused on the sample and are scanned by a galvanometer scanner. The generated CARS light is detected by a photomultiplier tube (PMT). PD, photodiode; BS, beam splitter; DM, dichroic mirror; F, filter; RL, relay lens; and OB, objective lens. (b) Photograph of the CARS rigid endoscope. (c) Photograph of the assembled rigid endoscope tube. (d) Exploded endoscope tube. The tube consists of outer cylinders, inner cylinders, a cap cylinder, a pair of relay lenses, and an objective lens. The pair of relay lenses is fixed by the inner cylinders. (e) The objective lens is screwed into the cap cylinder.

cross-correlation of the two laser pulses was detectable. Blue and red lines were observed before and after delivering the laser pulses with a 2 m single-mode fiber, respectively. Because of the group delay dispersion of the single-mode optical fiber, the timing of the two laser pulses was shifted by about 50 ps. For CARS imaging we had to adjust the optical delay to maximize the CARS signal. Since the large dispersion of the fiber reduced the overlapping period of the two laser pulses, the nonlinear effects in the fiber were not a severe problem. The coupling efficiencies of the pump and Stokes beams were 65% and 50%, respectively.

Biomedical Optics EXPRESS

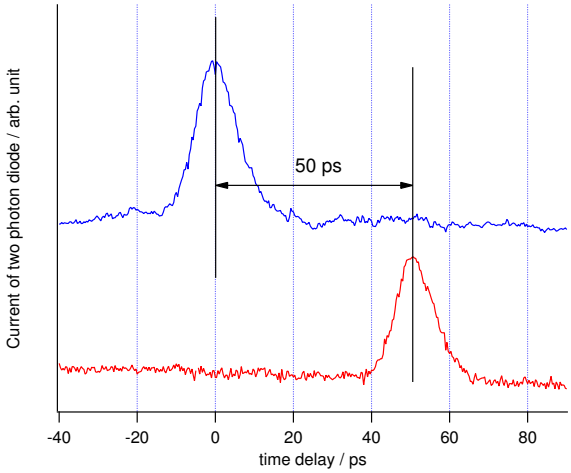

Fig. 2. Cross-correlation signals between two color laser pulses (709 and 888 nm) before (blue line) and after (red line) traveling through 2 m of single-mode fiber.

3.2. *Estimation of field of view, distortion, uniformity and spatial resolution*

To examine the field of view of the developed rigid endoscope, we observed 500×500-pixel transmission images of micrometer scales (Fig. 3) by scanning the galvanometer mirrors and using a Si photodiode placed at PD3 in Fig. 1(a). Figure 3(a) shows that the diameter of the field of view was 650 μm, which corresponds to a 450 μm × 450 μm square image. The distortion of the image was estimated by observing a micrometer grid scale (Fig. 3(b)). The average distances between the black grid lines on the red lines at the left, center and right were 6.69, 6.67 and 6.70 pixels, respectively. Those at top, middle and bottom drawn indicated with blue lines were 6.51, 6.45 and 6.48 pixels. Therefore, the obtained image showed pincushion distortion smaller than 0.91%. Figure 3(c) is a CARS image of 45 μm polystyrene beads. The average and standard deviation of the CARS intensity of each bead were 19.4 and 1.66, respectively, confirming that high uniformity (non-uniformity: 8.6%) was achieved. Figure 3(d) and (e) show a CARS image of 2 μm polystyrene beads and its CARS intensity profile to estimate the spatial resolution. The full-width at half maximum of the CARS intensity profile of a 2 μm polystyrene bead was 2.91 μm. Non-linear effect improved the spatial resolution of CARS image even though the Airy radii of excitation beams (λ = 709 and 888 nm, beam diameter = 2.0 mm) are 3.3 and 4.2 μm, respectively.

4. CARS endoscopic imaging of myelinated nerve in rat sciatic nerve

To demonstrate nerve imaging, CARS imaging of a rat sciatic nerve was performed using the developed endoscope. A myelinated nerve has a layered structure consisting of a neuronal axon, myelin sheaths, and Schwann cells. Since myelin sheaths have abundant phospholipids, myelinated nerves can be visualized by Raman imaging of the CH_2 symmetric stretching vibration of the lipid at 2845 cm^{-1}. A formalin-fixed sciatic nerve of a Sprague-Dawley rat purchased from Japan Lamb Co., Ltd. was prepared as a sample (Fig. 4(a)). The rat sciatic nerve was cut along the axis to observe the nerve fibers (yellow dotted circle in Fig. 4(a)), sandwiched between a cover slip and slide glass using a silicon spacer (2 mm thickness), and the gap was filled within phosphate buffered saline to prevent drying. Figure 4(b) and (c) show transmission and CARS images of the sciatic nerve, respectively. Individual fine nerve fibers were clearly detected in the CARS image of the lipid (arrow in Fig. 4(c)). The inset image indicated by the asterisk is a

Biomedical Optics EXPRESS

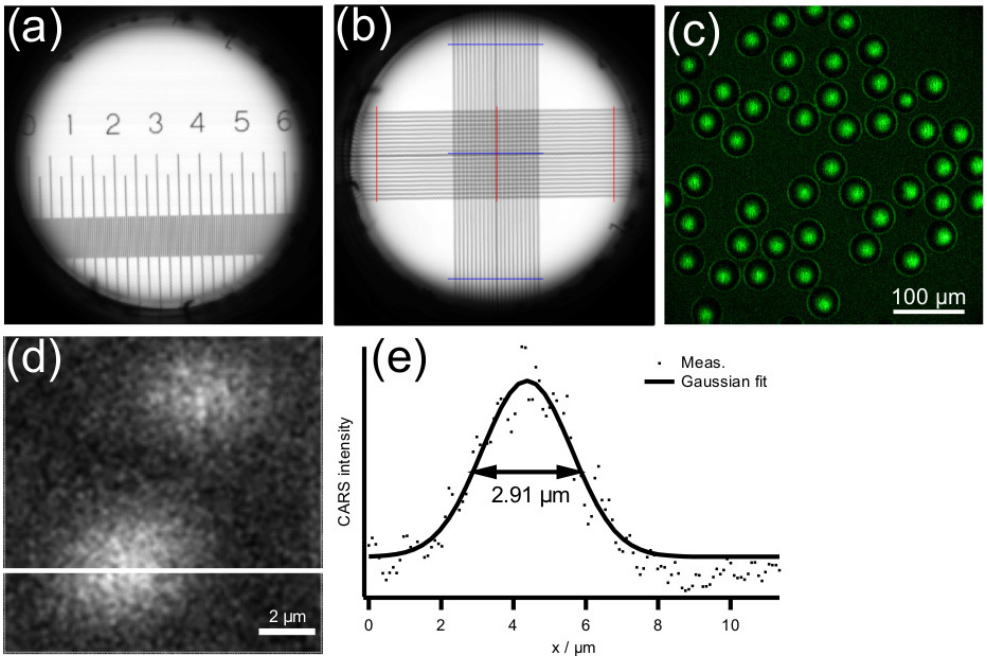

Fig. 3. Field of view of the rigid endoscope. (a) A transmission image of a micrometer scale. (b) A transmission image of a micrometer grid scale for evaluating the distortion of the imaging system. (c) A CARS image of 45 μm polystyrene beads. (d) A CARS image of 2 μm polystyrene beads. (e) A CARS intensity profile along the line in (d). The measured lateral profile (dots) and Gaussian fit (solid line) of a 2 μm polystyrene bead.

magnified view of the white square region in Fig. 4(c). The cross-sectional nerve structure of myelin sheaths surrounding the neuronal axon was also clearly visualized. At the sample position, the powers of the pump and Stokes beams were 30 mW and 15 mW, respectively. The number of pixels was 500×500, and the final image was obtained by accumulating 300 images at 2 s/image.

We consider that the non-uniformity of CARS intensity of nerve (Fig. 4(c)) is caused by the polarization dependency of CARS. It is known that the myelin sheath shows polarization dependency of CARS signal [34]. However, the image also includes the effect of epi-detection. Further investigations are required to identify nerve with high accuracy.

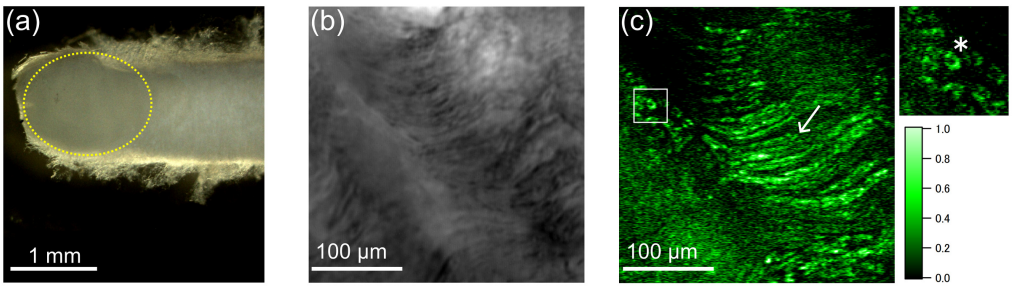

Fig. 4. Label-free imaging of rat sciatic nerve. (a) Photograph of prepared rat sciatic nerve. The sample was cut along the axis (yellow dotted circle). (b) Transmission and (c) CARS images inside of yellow dotted circle in (a). Fibrous (arrow) and circular (asterisk) structures of myelin sheaths are clearly shown.

Biomedical Optics EXPRESS

5. Discussion

The features of the developed CARS rigid endoscope are 2.91 μm spatial resolution, 650 μm diameter field of view (450 μm × 450 μm square image), low distortion and high CARS intensity uniformity. The developed rigid endoscope is not so high resolution comparing with the previously reported CRS endoscopic systems [22–28]. However, our system provides the largest imaging field of view. For intraoperative purpose, not imaging of individual nerve cells, but identification of nerve distribution is demanded. Therefore, an endoscope with large field of view is suitable for robot-assisted surgery. Relay lenses with shorter focal length will enlarge the field of view.

We succeeded in label-free imaging of a rat nerve using the developed rigid endoscope. However, a large number of accumulations, that is, a long exposure time, was required for obtaining an image. As imaging within several seconds is required to achieve intraoperative use, the imaging speed must be improved. Tight focusing and spatial overlapping of the two laser beams on the sample will improve the imaging speed.

Chromatic aberration, which reduces the degree of spatial overlapping of the two beams, is a major limiting factor for high-speed, non-linear Raman imaging. Although chromatic aberration of a conventional endoscope reduces the resolution and imaging quality, in non-linear Raman imaging it decreases the signal level. In the present system, since the two laser pulses were delivered with a single-mode fiber, they were completely overlapped at the exit end of the fiber. To reduce the chromatic aberrations, we used a reflective fiber collimator and achromatic relay and objective lenses. Nevertheless, we observed some chromatic aberration of the developed endoscope at the wavelengths use for nerve imaging.

We estimated the longitudinal (i.e., along the optical axis) chromatic aberration of the developed system by measuring the longitudinal distance between the focal spots of the two laser beams. Figure 5 shows the normalized two-photon absorption signals of the two excitation laser beams. The solid and broken lines are the results for the pump (λ = 709 nm) and Stokes (λ = 888 nm) beams, respectively. The peak of the curve indicates the position of the focus, and the focal positions of the two beams were shifted by 21 μm. In order to detect the focal spots, we also used a TPD. Because the current of the TPD is proportional to the square of the intensity, it is maximized at the focus where the photon density is the highest. The curves in Fig. 5 were obtained by scanning the TPD with a z-axis stepping motor stage (OSMS80-20ZF, Sigmakoki) along the optical axis of the endoscope around the sample position.

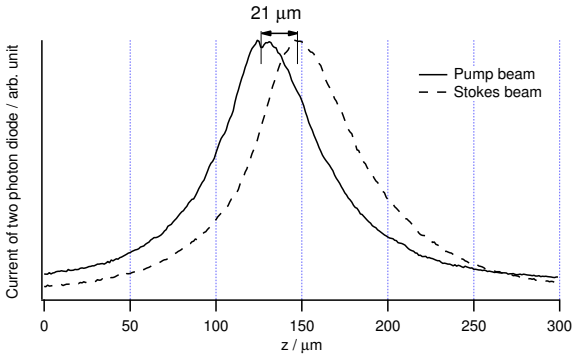

Fig. 5. Longitudinal focus positions of pump (709 nm) and Stokes (888 nm) laser beams. The focus difference between the two laser beams was 21 μm.

Since longitudinal aberration reduces CARS intensity, we numerically estimated the effect of correction of longitudinal aberration on the CARS intensity. The CARS intensity is proportional to the product of f_p^2 and f_s when the phase matching condition is satisfied. In the case of a highly

Biomedical Optics EXPRESS

scattering sample, the obtained CARS signal depends on the surface intensities of the excitation beams and is expressed by

$$I_{\mathrm{CARS}}(a, z, z') \propto 2\pi\phi \int f_p(a, r, z)^2 f_s(a, r, z - z') r dr. \quad (1)$$

Here, f_p and f_s are three-dimensional intensity distributions near the focal points of the ω_{p} and ω_{s} beams, respectively [35], ϕ is a collection factor of the backscattered light, a is a beam radius, r is the radial coordinate on the focal plane, z is the coordinate along the optical axis, and z' is the longitudinal focus difference between the two beams.

Figure 6(a) shows CARS signal intensities versus the longitudinal focus difference between the pump and Stokes beams (z') with the current objective lens (f = 7.5 mm). Since Eq. (1) is a function of z, we gave the z that maximizes the CARS intensity to plot individual points in Fig. 6. The vertical axis is normalized by I_{CARS} (a = 1.0 mm, z' = 0 μm), where a = 1.0 mm is the beam radius of the present system. It was found that increasing the beam radius and reducing chromatic aberration increased the CARS intensity. Figure 6(b) also shows the enhancement factor of the CARS intensity with increasing beam radius (vertical axis is similar to that in Fig. 6(a)) in the case of an f = 5 mm objective. The CARS signal intensity with corrected chromatic aberration (z' = 0), enlargement of the beam radius to 2.0 mm, and a tight focusing objective lens (f=5.0 mm) was 90 times as large as the CARS signal intensity obtained with the current conditions ((a, z', f) = (1.0 mm, 21 μm. 7.5 mm)). In the present system, nerve imaging required 600 seconds; however, surgeons cannot wait for such a long time. Increasing the CARS intensity by a factor of 90 will reduce the imaging time to several seconds.

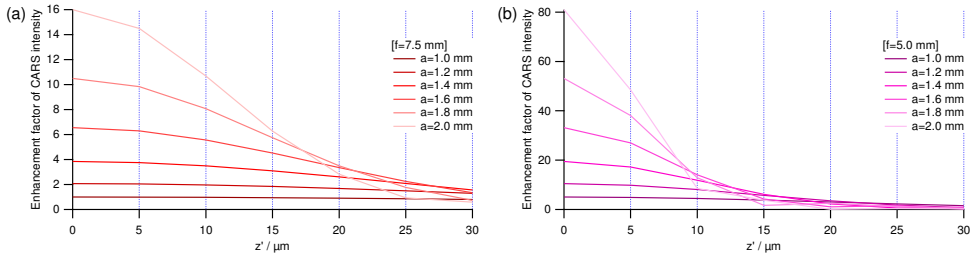

Fig. 6. The effect of beam radius (a) and longitudinal focus difference (z') on CARS intensity using an f = 7.5 mm objective lens (a) and an f = 5.0 mm objective lens (b).

6. Conclusion

We developed a CARS rigid endoscope for intra-operative nerve imaging and demonstrated CARS imaging of a rat sciatic nerve. Myelinated nerves were clearly visualized with the CH_2 symmetric stretching at 2845 cm^{-1}. The developed endoscope tube had a diameter of 12 mm and a length of 270 mm. The excitation beams were delivered with a single-mode optical fiber. An image was obtained by scanning the beams with galvanometer mirrors and detecting the backscattered CARS signal with a photomultiplier tube. The diameter of the field of view was 650 μm, and a uniform CARS intensity in the whole field of view was confirmed. In the present system, the imaging time required ten minutes. However, from the results of numerical simulation, imaging within several seconds should be achievable by correction of longitudinal chromatic aberration and tightly focusing the beams. This technique is applicable to non-destructive, high-speed, highly molecule-specific imaging, in particular nerve imaging, and will contribute to further improvements in the safety of endoscopic surgery and the QoL of patients.

Biomedical Optics EXPRESS

Funding

Japan Agency for Medical Research and Development (AMED) under Collaborative Research Based on Industrial Demand "In Vivo Molecular Imaging: Towards Biophotonics Innovations in Medicine" (15im0402007h0005); Japan Society for the Promotion of Science (JSPS) Grant-in-aid for Scientific Research B (17H0279307).

Acknowledgement

The authors acknowledge Prof. T. Takamastu (Kyoto Prefectural University of Medicine) and Mr. A. Hasegawa (Olympus) for fruitful discussions. The authors also acknowledge Mr. Y. Sakaguchi (Osaka University) for mechanical design of the endoscope tube.

Disclosures

The authors declare that there are no conflicts of interest related to this article.